NUMERICAL STUDY OF FLOWS OVER LAUNCH VEHICLES WITH VARIOUS FAIRING BY SECOND-MOMENT CLOSURE DETACHED-EDDY SIMULATION

Quanzheng Li^{1,2}, Gang Wang^{1,2*}, Mengzhu Qin^{1,2}, Lincheng Xu^{1,2}

School of Aeronautics, Northwestern Polytechnical University, Xi'an 710072, China National Key Laboratory of Aircraft Configuration Design, Xi'an 710072, China * Corresponding Author: wanggang@nwpu.edu.cn

Abstract

During the transonic flight of a launch vehicle with fairing (hammerhead configuration), buffeting usually occurs due to the strong nonlinear unsteady flow characteristics near the fairing and booster joints, including oscillating shock waves, massive flow separation and reattachment. Naturally, the fairing geometry is critical for the evolution of the mentioned flow physics and the resulting buffeting load on the hammerhead launch vehicle. In this paper, a recently developed second moment closure detached-eddy simulation (DES) method is used to investigate the influence of the fairing geometric parameters on the buffeting load of the NASA hammerhead launch vehicle canonical model. The second-moment closure DES method is preferred because it has been verified to be superior to the traditional eddy viscosity model-based DES method in the prediction of buffeting load on the hammerhead launch vehicle. Vehicle configurations with different fairing cylinder lengths and boat angles are considered in simulations and compared to the baseline model. The results show that the low-frequency buffeting load on the booster can be significantly reduced by decreasing the fairing boat angle to block the downstream separation bubble bumping. In addition, increasing the fairing cylinder length can reduce not only the full-frequency buffeting load on the booster but also the buffeting load caused by shock wave oscillation on the fairing by attenuating the perturbation backscatter downstream. These findings could be quite useful in developing effective anti-buffeting techniques.

Keywords: Launch vehicle, Transonic buffeting, Massive flow separation, Detached-eddy simulation, Second moment closure.

1. General Introduction

Buffeting usually occurs in the transonic flight stage of a launch vehicle due to some nonlinear unsteady flow characteristics, including oscillating shock waves, massive flow separation and reattachment [1]. The fluctuation load generated by buffeting will significantly impact flight stability, devices, and sensors. Thus, the accurate prediction of buffeting is an indispensable part of launch vehicle design. For a launch vehicle with fairing (hammerhead configuration), the presence of the large-diameter fairing will form a massively separated region on the downstream booster [2], which will produce a dominant buffeting load and affect the shock buffeting loads at the vehicle stage joints through perturbation propagation. Naturally, fairing geometry is critical for the flow evolution around a launch vehicle, so it is significant to study the influence of fairing geometric dimensions on the buffeting load of a hammerhead launch vehicle.

Flow over the hammerhead model is characterized by wall turbulence with a high Reynolds number, which means that the multi-scale characteristics of the vortex structure are more obvious. Thus, the cost of using eddy resolution methods such as direct numerical simulation (DNS) and large eddy simulation (LES) to resolve the flow characteristics in the high Reynolds number wall turbulence is unaffordable. In order to reduce the calculation cost of wall turbulence with a high Reynolds number, the Reynolds-averaged Navier–Stokes method is widely used in aerospace engineering to simulate the time-averaged flow [3,4,5]. However, the buffeting flow around the launch vehicle holds strongly

unsteady characteristics. Thus, the RANS method is not capable of predicting and simulating launch vehicle fluctuation load. Considering the requirement of high fidelity and high efficiency in predicting turbulent flow over the launch vehicle, the hybrid RANS/LES method is an alternative. Detached-eddy simulation (DES) [6] method is a typical and widely used hybrid RANS/LES method, which adopts RANS simulation in boundary layer flow near the wall and LES simulation in the flow far away from the wall. The DES method is first proposed by Spalart under the Spalart–Allmaras (SA) turbulence model, and then detached DES (DDES) [7] and improved DDES (IDDES) [8] are further developed to avoid the grid-induced separation (GIS) and logarithmic layers mismatched (LLM) issues of the original DES. The DES method is obtained by trimming the dissipation from the RANS model, which is naturally affected by its underlying RANS model. Various DES methods under different turbulence models are proposed to improve the capacity of complex flows: Strelets [9] developed the corresponding DES based on the shear stress transport (SST) model, and Wang [10] and Li [11] developed the DES under the second-moment closure Reynolds stress model (RSM).

Some studies investigated the fluctuation loads on the hammerhead configuration by using the DES method. Liu [12] used SA-based DES to investigate the flow around the NASA hammerhead launch vehicle model [13]. The linear eddy-viscosity model is not good at predicting the strong shear flow in the free shear layer shedding from the fairing and delays in predicting the instability process of the free shear layer. Recent studies show that second-moment closure DES is superior to the traditional eddy viscosity model-based DES in the prediction of hammerhead model buffeting [10,11]. Therefore, the second-moment closure DES is adopted for current work. The NASA hammerhead launch vehicle model [13] has been widely studied [12,14,15,16] and is chosen as the baseline model for this work. Two additional hammerhead models that change the fairing boat angle and the fairing cylinder length are used to study the influence of fairing geometric dimensions on the buffeting load of the hammerhead launch vehicle model.

2. Geometry Configuration

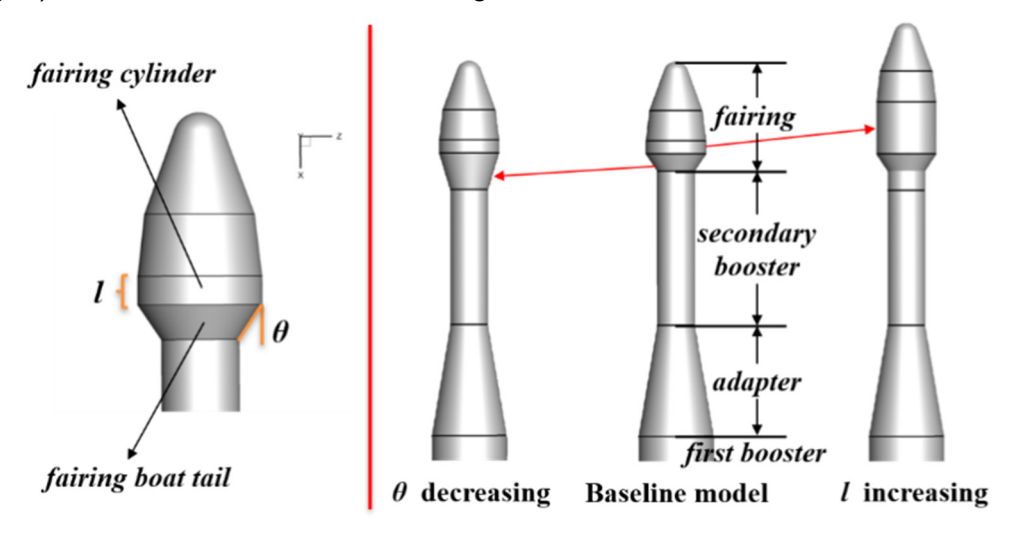


Figure 1 – Geometry of various hammerhead launch vehicle configurations.

3. Numerical Method

3.1 Governing Equations

The baseline solver adopted in this work is an in-house hybrid-unstructured-mesh-based 3D Navier-Stokes solver (HUNS3D) [17]. It has been successfully implemented in lots of research domains, such as complex turbulent flow simulation [18], buffeting flow simulation [12], sonic boom prediction [19], multidisciplinary coupling simulation [20], and so on. HUNS3D adopts the finite volume method to solve the following Navier-Stokes (N-S) equations in the integral form.

$$\frac{\partial}{\partial t} \iiint_{\Omega} \mathbf{Q} dV + \iint_{\partial \Omega} \mathbf{F}(\mathbf{Q}) \cdot \mathbf{n} dS = \iint_{\partial \Omega} \mathbf{G}(\mathbf{Q}) \cdot \mathbf{n} dS \tag{1a}$$

$$\mathbf{F}(\boldsymbol{Q}) \cdot \boldsymbol{n} = (\boldsymbol{V} \cdot \boldsymbol{n}) \begin{pmatrix} \bar{\rho} \\ \bar{\rho} \tilde{u} \\ \bar{\rho} \tilde{v} \\ \bar{\rho} \tilde{H} \end{pmatrix} + \bar{p} \begin{pmatrix} 0 \\ n_{x} \\ n_{y} \\ n_{z} \\ 0 \end{pmatrix}$$
 (1b)

$$\mathbf{G}(\boldsymbol{Q}) \cdot \boldsymbol{n} = \begin{pmatrix} 0 \\ \bar{\tau}_{xx} \\ \bar{\tau}_{yx} \\ \bar{\tau}_{zx} \\ \tilde{u}\bar{\tau}_{xx} + \tilde{v}\bar{\tau}_{xy} + \tilde{w}\bar{\tau}_{xz} - \bar{q}_{x} \end{pmatrix} n_{x} + \begin{pmatrix} 0 \\ \bar{\tau}_{xy} \\ \bar{\tau}_{yy} \\ \bar{\tau}_{zy} \\ \tilde{u}\bar{\tau}_{yx} + \tilde{v}\bar{\tau}_{yy} + \tilde{w}\bar{\tau}_{yz} - \bar{q}_{y} \end{pmatrix} n_{y} + \begin{pmatrix} 0 \\ \bar{\tau}_{xz} \\ \bar{\tau}_{yz} \\ \bar{\tau}_{zz} \\ \tilde{u}\bar{\tau}_{zx} + \tilde{v}\bar{\tau}_{zy} + \tilde{w}\bar{\tau}_{zz} - \bar{q}_{z} \end{pmatrix} n_{z} \quad (\text{ 1c })$$

Where ${m Q}=(ar
ho\ ar
ho ar
ho\ ar
ho ar
ho\ ar
ho ar
ho \ ar$

3.2 Turbulence Model

The turbulence stress $\bar{\rho}\tilde{R}_{ij}$ is an unclosed term of Navier-Stokes equations, which needs to be computed by a turbulence modeling. In this work, the second-moment closure detached-eddy simulation (DES) is adopted by using the Reynolds stress model (RSM). The relevant equations are summarized as follows.

$$\frac{\partial}{\partial t} \left(\bar{\rho} \tilde{R}_{ij} \right) + \frac{\partial}{\partial x_{b}} \left(\bar{\rho} \tilde{u}_{k} \tilde{R}_{ij} \right) = \bar{\rho} P_{ij} + \bar{\rho} \Pi_{ij} - \bar{\rho} \varepsilon_{ij} + \bar{\rho} D_{ij} \tag{2}$$

$$\frac{\partial}{\partial t}(\bar{\rho}\omega) + \frac{\partial}{\partial x_k}(\bar{\rho}\tilde{u}_k\omega) = \frac{\gamma}{v_t}\bar{R}_{ij}\frac{\partial \tilde{u}_i}{\partial x_j} - \beta_\omega\bar{\rho}\omega^2 + \frac{\partial}{\partial x_k}\left[(\bar{\mu} + \sigma_\omega\mu_t)\frac{\partial\omega}{\partial x_k}\right] + 2(1 - F_1)\frac{\bar{\rho}}{\omega}\sigma_{\omega 2}\frac{\partial\tilde{k}}{\partial x_k}\frac{\partial\omega}{\partial x_k}$$
(3)

The terms on the right-hand side of Eq.(2) are the production term of $\bar{\rho}\tilde{R}_{ij}$, the redistribution term, the dissipation term, and the diffusion term, respectively. The production term $\bar{\rho}P_{ij} = -\left(\partial_i\tilde{u}_k\bar{\rho}\tilde{R}_{kj} + \partial_j\tilde{u}_k\bar{\rho}\tilde{R}_{ki}\right)$ is a closed term that can be computed by solution variables. The others are the unclosed terms that need to be modeled. Among them, the dissipation term $\bar{\rho}\varepsilon_{ij}$ is calculated by the following formula.

$$\bar{\rho}\varepsilon_{ij} = \frac{2}{3}\bar{\rho}\frac{\tilde{k}^{1.5}}{l_{DES}}\delta_{ij} \tag{4}$$

Where \tilde{k} is the turbulent kinetic energy that can be determined by the half trace of Reynolds stress $\tilde{k} = \tilde{R}_{kk}/2$ according to the definition. l_{DES} is the DES length scale that is calculated by the following improved delayed DES scheme.

$$l_{DES} = \bar{f}_d (1 + f_e) l_{RANS} + (1 - \bar{f}_d) l_{LES}$$
 (5)

Where $l_{RANS} = \sqrt{\bar{k}}/C_{\mu}\omega$ is the RANS length scale, and $l_{LES} = C_{DES}\Delta$ is the LES length scale. C_{μ} is a constant, $C_{\mu} = 0.09$. C_{DES} is a parameter that affects the subgrid dissipation in the LES region. It requires to be calibrated by using canonical turbulence case (such as the decay of isotropic turbulence) to adapt the dissipation level of a specific solver. Details of the calibration process can be found in reference [10]. \bar{f}_d in Eq.(5) is a shielding function to ensure that RANS simulation is used inside the boundary layer and LES simulation is turned on outside. f_e is an elevating function, which is turned on appropriately below the logarithmic layer to avoid an excessive reduction of turbulent stress that leads to the logarithmic layer mismatched issue. Further details of empirical functions \bar{f}_d and f_e can be found in reference [8].

The other unclosed terms on the right side of Eq.(2), the redistribution term and the diffusion term, have different closures depending on the RSM model selected. The RSM model used in this work is the Speziale-Sarkar-Gatski (SSG)/Launder–Reece–Rodi (LRR)-ω RSM model presented by the German Aerospace Center (DLR) [21]. It blends the advantages of the SSG-RSM model and LRR-RSM model for the simulation of equilibrium turbulence far away from the wall and the near-wall turbulence. Details of the redistribution and diffusion terms modeling can be found in reference [21].

3.3 Numerical Scheme And Computational Mesh

All cases are computed by the HUNS3D solver. RSM model-based IDDES (RSM-IDDES) method is adopted as the turbulence modeling. Cell-centered finite volume method (FVM) is used for numerical discretization. Roe discretization scheme is used to calculate the discretized convective flux $\mathbf{F}(Q) \cdot \mathbf{n} dS$, and central scheme is used to compute the discretized viscous flux $\mathbf{G}(Q) \cdot \mathbf{n} dS$. The Barth's interpolation is adopted for second-order reconstruction of the mesh face value. The Green-Gauss method is used to obtain the solution gradient for the interpolation. Lower-Upper Symmetric Gauss-Seidel (LU-SGS) relaxation-based full implicit dual-time backward-Euler scheme is implemented for steady flow simulation. The setup of numerical scheme is summarized in Table 1

Table 1 – Computational setup of numerical scheme.

Items	Description
turbulence modeling	RSM model-based IDDES
discretization method	cell-centered finite volume method
discretization order	second-order by Barth's interpolation
gradient computing method	Green-Gauss method
convective flux scheme	Roe scheme
viscous flux scheme	central scheme
time-advancing scheme	full implicit dual-time scheme
linear system solving method	LU-SGS

The computational domain of the cases is a half-cylinder with a diameter of 1640D (D is the diameter of the first booster) and a length of 4100D (as shown in Figure 2). Outer boundary condition of the computation domain is pressure far field with non-reflecting condition, and inner boundary condition is viscous wall boundary. Geometry of the hammerhead configuration investigated in the work is axial symmetry, thereby a symmetric boundary condition is adopted for half-model calculation to reduce the computational costs.

The computational mesh adopted in the work is an unstructured hybrid mesh. The structured grid is surrounded by the hammerhead configuration to capture the flow field details, and the unstructured mesh is filled in the other region to reduce the total amount of computational mesh. Local refinement is performed in the regions downstream of the fairing and the junction of the first booster and the adapter to finely capture the massively separated flow downstream of the fairing and the shock wave on the first booster. The first layer height of the mesh is guaranteed to be $y^+ < 1$, and the growth rate in the boundary layer is 1.21. 210 points are uniformly arranged in the circumferential direction, and 600

points are arranged in the streamwise direction. In particular, the grid points in the focus region between the beginning of the fairing cylinder and the first stage booster are 470. The mesh adopted in this work is further refined on the basis of the high-density mesh in reference [12] and the mesh in reference [10]. The mesh resolution sufficiency of resolving the fluctuation flow field around the hammerhead configuration have investigated in the previous references under the same solver, thus it will not covered again in this work. The total cell number of the mesh is about 24.388 million of the half-model.

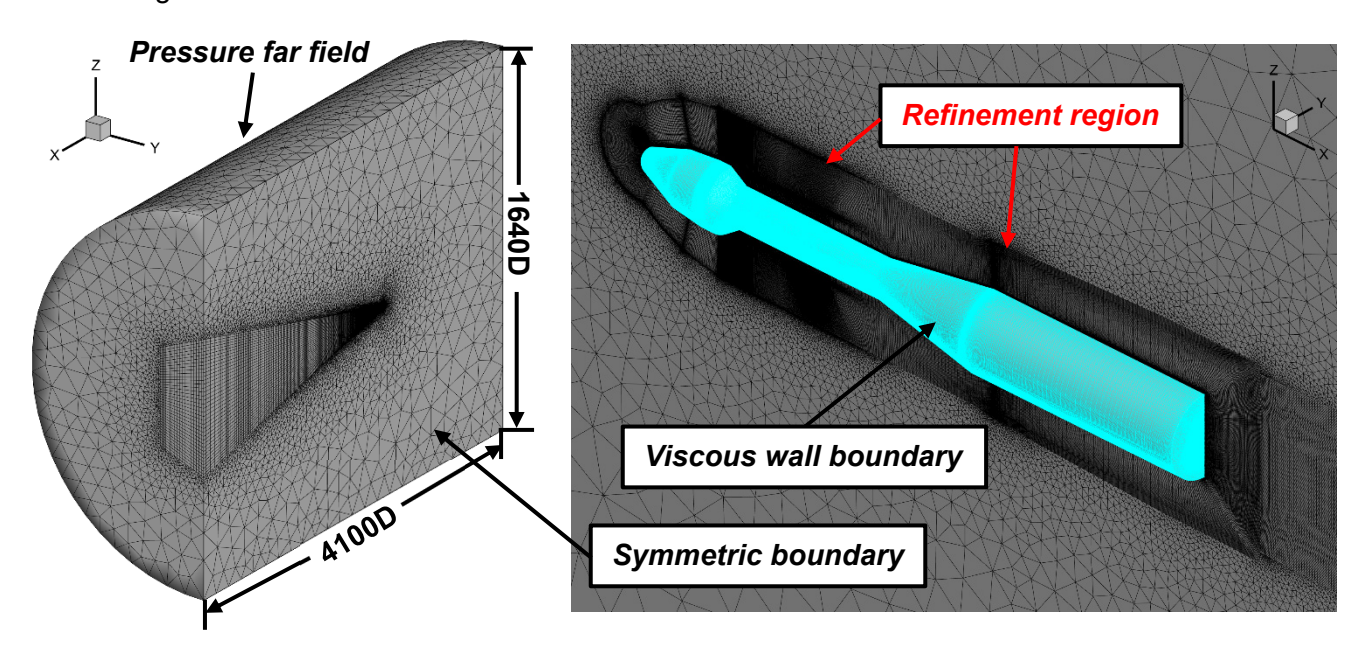


Figure 2 – Computational mesh and boundary conditions of the hammerhead configuration.

The mesh topology and mesh scale distribution of the other two configurations is consistent with the baseline configuration (as shown in Figure 3) to eliminate the influence of the grid-scale on the computational results. The latter part of the launch vehicle hammerhead and the front part of the fairing are maintained in the mesh re-division. The adjustment of the mesh is only in the region near the fairing (indicated by the red frame in Figure 3), whereas the mesh scale distribution in all directions ensures it is consistent with the baseline model. The total cell number of the mesh of the θ decreasing configuration is about 24.386 million, and the I lengthen configuration is about 28.615 million.

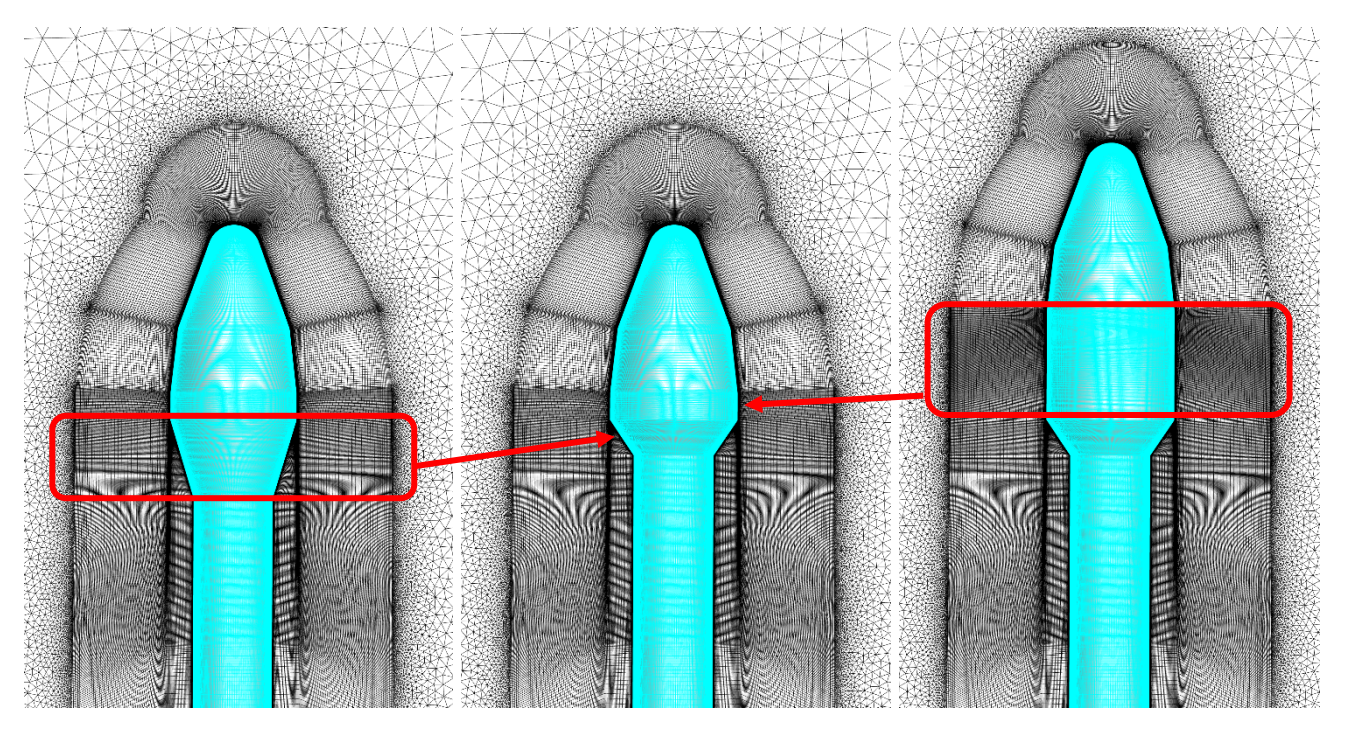


Figure 3 – Computational mesh of hammerhead configurations with various fairing geometry.

4. Results and Discussion

Figure 4 shows the numerical schlieren of density gradient magnitude over the baseline model to illustrate the production mechanism of transonic buffeting on the hammerhead configuration. As shown in Figure 4, there exist many complex flow patterns around the hammerhead launch vehicle configuration, such as shock wave and expansion wave system at the junction of each stage, flow separation and attachment, free shear layer shedding from the fairing, and detached turbulent vortex structures generated by the free shear layer broken due to the Kelvin-Helmholtz instability. The detached-eddies downstream of the fairing carry certain fluctuation energy and impact the secondary booster, which is a source of buffeting on the hammerhead launch vehicle configuration. The second source of buffeting is the oscillation of shock waves. The shock wave oscillation on the fairing is mainly caused by the shock wave boundary layer interaction, and the shock wave oscillation on the first booster is also affected by the turbulent vortex convecting from the upstream.

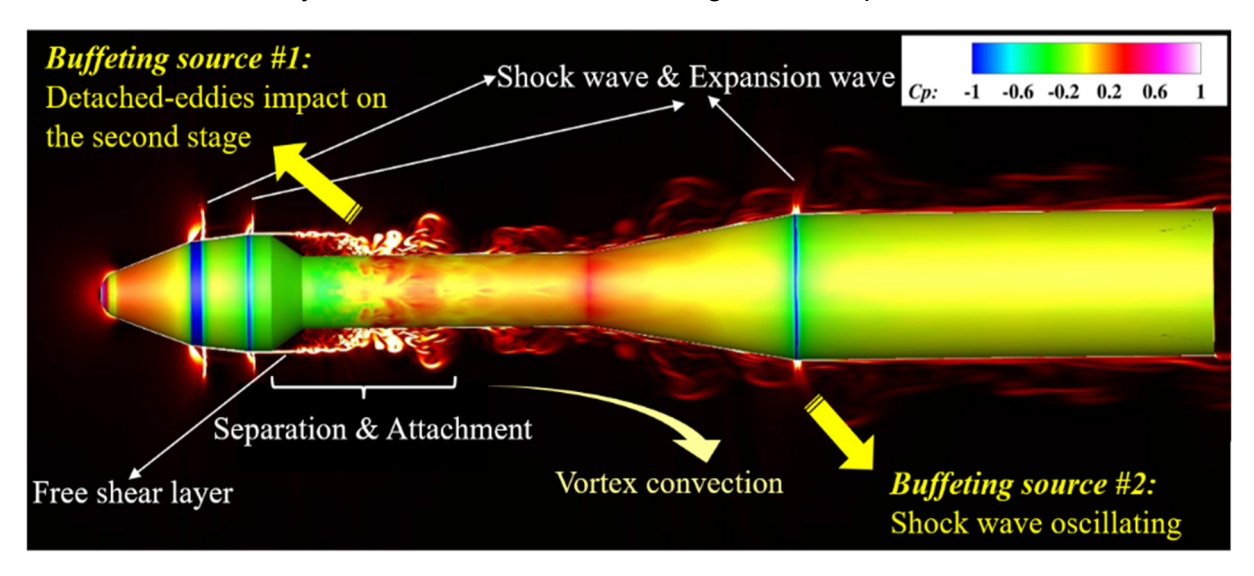


Figure 4 – Illustration of transonic buffeting on the hammerhead launch vehicle model. Flow field is depicted by the density gradient magnitude. Wall contour is the pressure distribution.

Figure 5 shows the Mean pressure (Cp_{avg}) and mean fluctuation pressure (Cp_{rms}) on the wall of the baseline configuration. The numerical results are compared with the experimental measurements conducted by Ames research centers [13]. The Cp_{avg} predicted by numerical computation is consistent with the experimental data, and the variations of Cp_{avg} in the shock/expansion wave systems at each stage connections and the massive separation region downstream of the fairing are accurately reproduced by RSM-IDDES.

Figure 5(b) compares the Cp_{rms} obtained by numerical computation and experimental measurement. The Cp_{rms} on the surface of the secondary booster downstream of the fairing and the connection position of the first booster are significant, which correspond with the two buffeting sources of hammerhead configuration. Due to the experimental measurement of Cp_{rms} being filtered, the calculated Cp_{rms} (unfiltered) are significantly larger than the experimental data. To compare with the experimental data appropriately, a bandpass (10-600Hz) filtering is performed on the numerical data according to the experimental filter. The filtered Cp_{rms} obtained by numerical computation are almost consistent with the experimental data, not only referring to the peak level but also the peak location. The peak level and location of Cp_{rms} downstream of the fairing correspond to the fluctuation energy contained in the turbulent vortex structures and the impact point position of the shear layer on the surface, respectively. Accuracy predictions of them demonstrate the capacity of RSM-IDDES to investigate the buffeting flow on the hammerhead launch vehicle configuration.

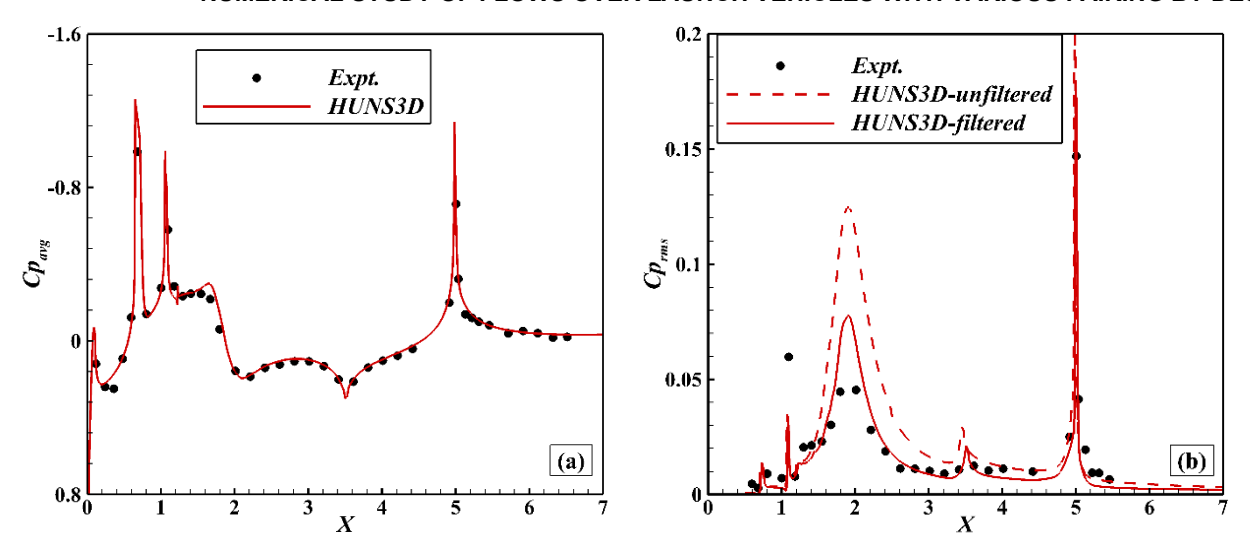
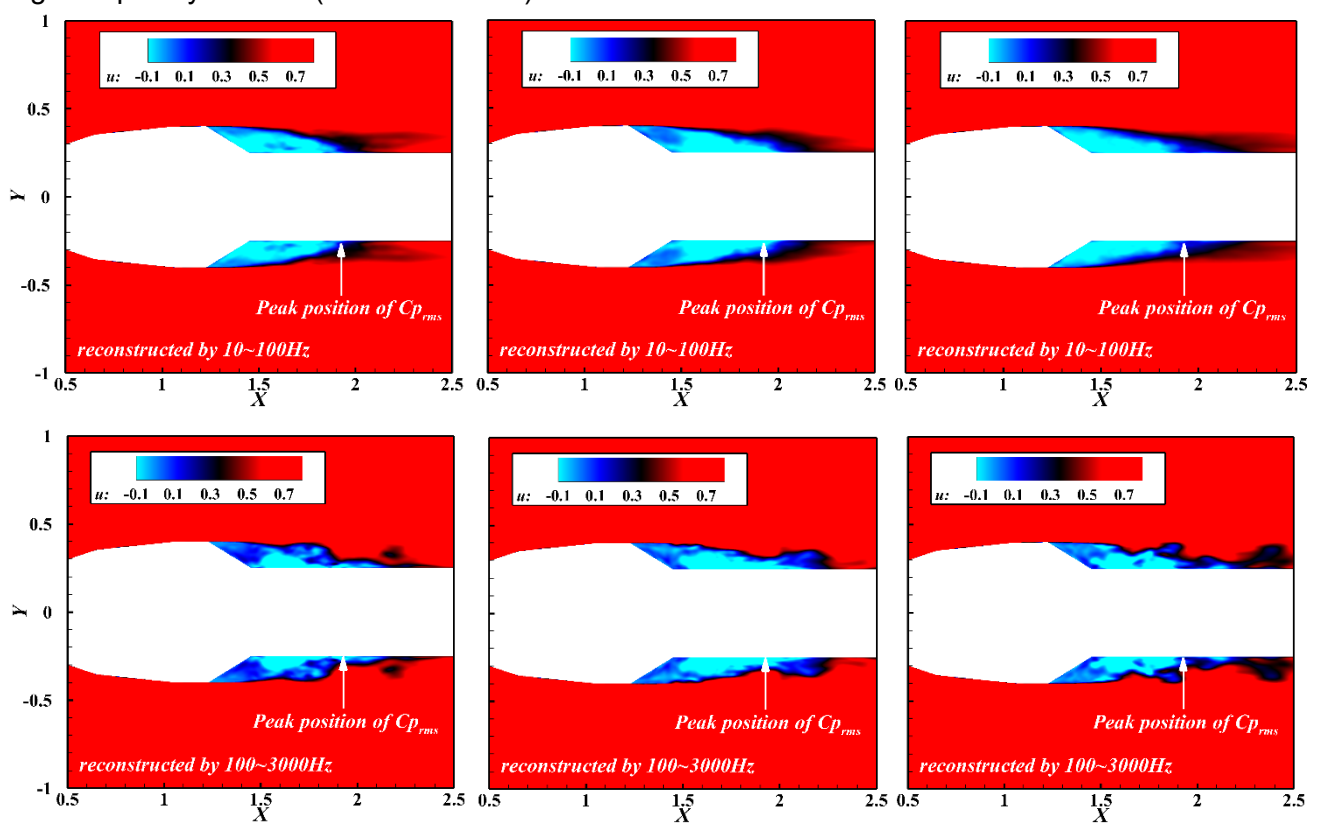


Figure 5 – Mean pressure (Cp_{avg}) and mean fluctuation pressure (Cp_{rms} , the root-mean-square of the fluctuation pressure) distribution along the generatrix of the baseline hammerhead configuration. (left: Cp_{avg} , right: Cp_{rms}).

The fairing geometry dimensions of the hammerhead launch vehicle will directly affect the fluctuation loads on the downstream secondary booster. It is necessary to investigate the production mechanism of fluctuation loads downstream of the fairing. The flow field downstream of the fairing is analyzed in frequency domain, and the flow field modes in different range of frequency domain are reconstructed to obtain the flow field modes in various frequency ranges. To promote the comprehensibility of the flow mode evolution process in each frequency domain, the averaged flow field is superposed to each frequency domain mode.

Figure 6 shows the flow fields reconstructed by various frequency domains at a series of instantaneous. The fluctuation load on the secondary booster is mainly generated by the following three flow modes: the pumping of the separation bubble downstream of the fairing dominated by the low-frequency domain (10~100Hz); the flapping of free shear layer dominated by the medium-frequency domain (100~3000Hz), and the striking of small-scale vortex structures dominated by the high-frequency domain (3000~10000Hz).



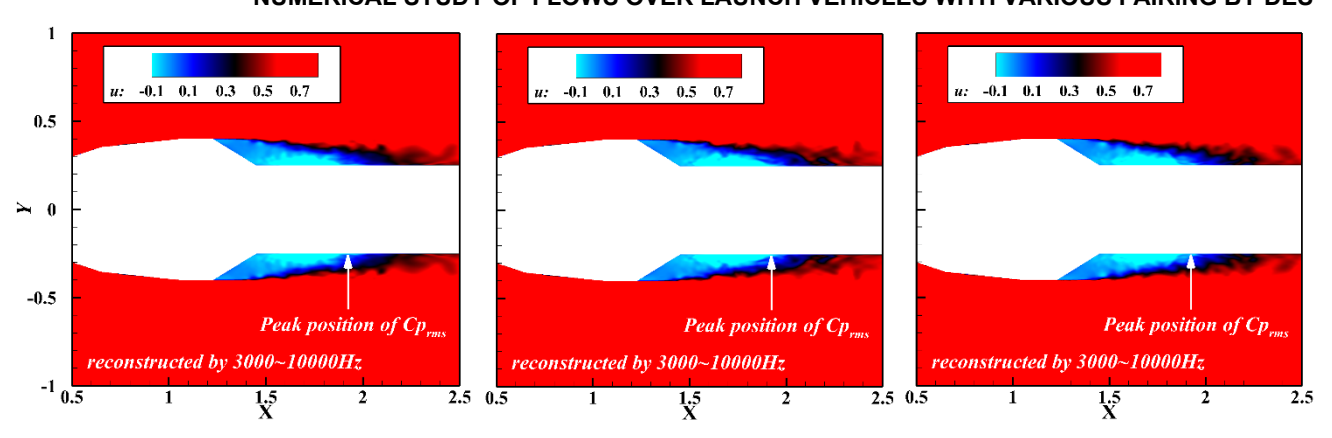


Figure 6 – Flow fields reconstructed by various frequency domains (superposed by the averaged flow field) at a series of instantaneous. First line: Flow fields reconstructed by 10~100Hz; Second line: Flow fields reconstructed by 100~3000Hz; The last line: Flow fields reconstructed by 3000~10000Hz.

Figure 7 shows the fluctuation loads on the various hammerhead configurations, and Figure 8 performs a circumferential average of the fluctuation pressure. For the three hammerhead launch vehicle configurations investigated in this study, the regions with significant fluctuation pressure are all the junction region of the first booster stage and the annular region on the second booster downstream of the fairing.

As shown in Figure 7, the geometric dimensions of the fairing mainly affect the fluctuation pressure on the fairing and its downstream annular region, while it almost holds little effect on the fluctuation pressure of the first booster. Decreasing the fairing boat angle and increasing the length of fairing cylinder can both reduce the fluctuation pressure on the annular region downstream the fairing. In addition, increasing the length of the fairing cylinder can also attenuate the buffeting load on the fairing. A more quantitative comparison is shown on the circumferential average of the surface fluctuation pressure (Figure 8).

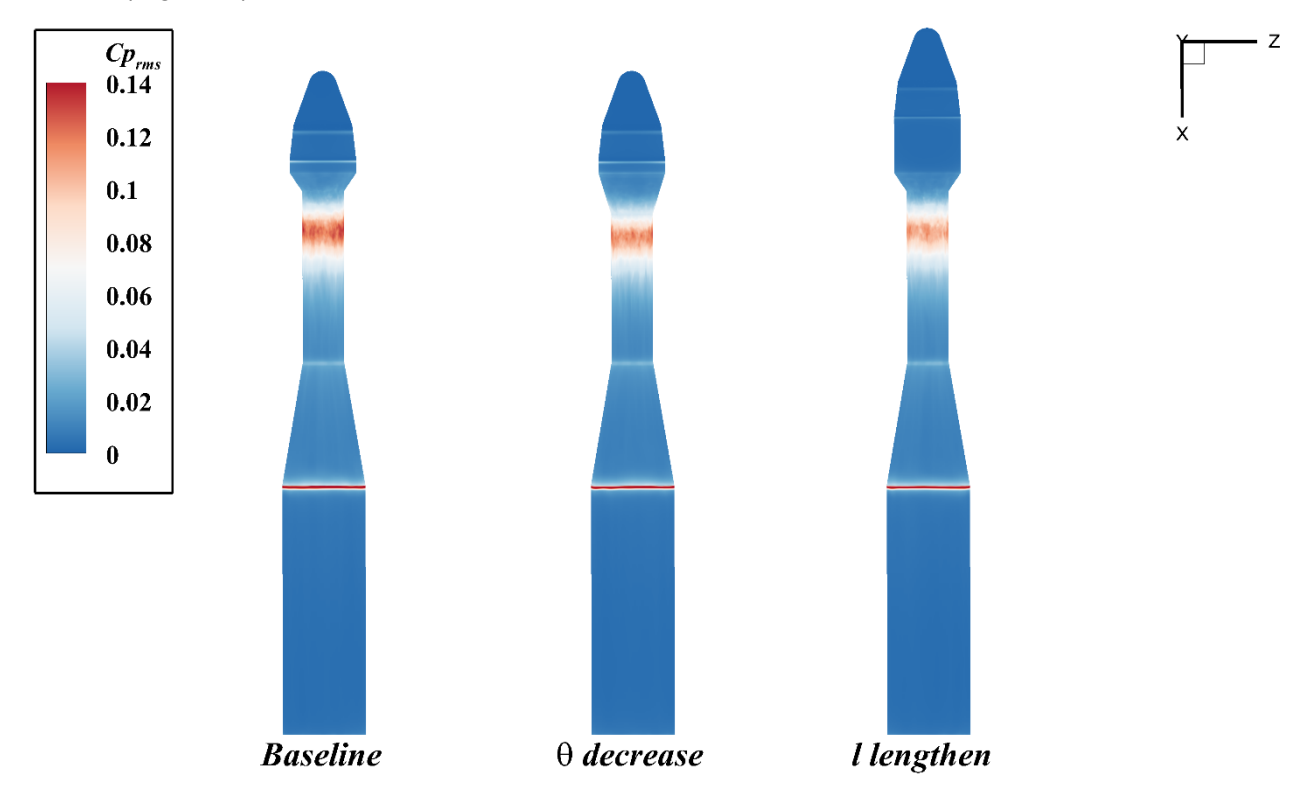


Figure 7 – Fluctuation loads (Cp_{ms}) distribution on the surface of hammerhead launch vehicle configurations with various fairing geometry.

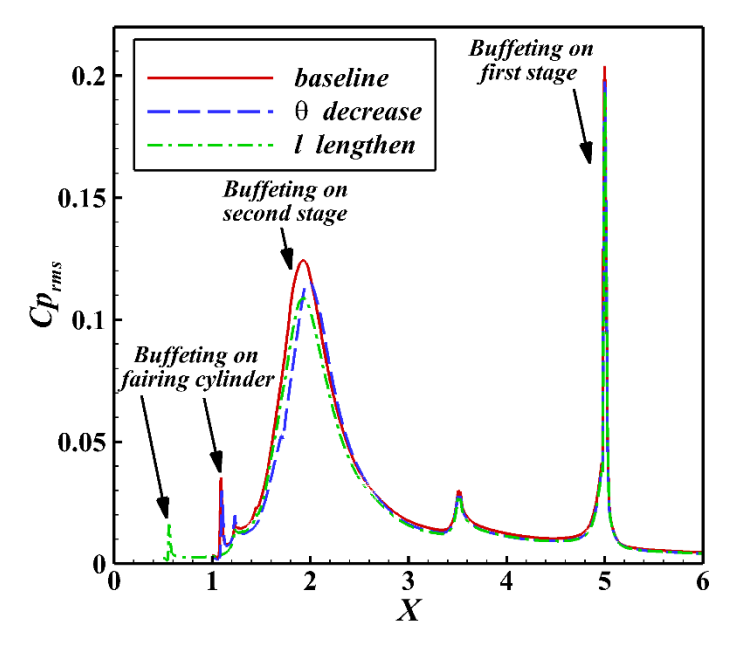


Figure 8 – Circumferential average of the fluctuation load (Cp_{rms}) distribution on the surface of hammerhead launch vehicle configurations with various fairing geometry.

The power spectrum density (PSD) at the peak of the fluctuation pressure downstream of the fairing is extracted (as shown in Figure 9) to further analyze the influence of fairing geometry dimensions on the fluctuating load. The geometric dimensions of the fairing have different influences on the fluctuation pressure in various frequency domains. According to the previous investigation of flow modes, the frequency domain is divided into the following three sub-domains: low-frequency domain (10~100Hz) of the separation bubble pumping mode, medium-frequency domain (100Hz~3000Hz) of the free shear layer flapping mode, and high-frequency domain (3000Hz~10000Hz) of the detached eddy striking mode.

The fairing boat angle on the fluctuation pressure is mainly reflected in the low-frequency domain. The decrease of boat angle of the fairing will compress the space of the downstream separation bubble and block the pumping movement of the separation bubble, thus reducing the fluctuation pressure in the low frequency domain on the secondary booster downstream of the fairing. On the other side, the influence of the length of the fairing cylinder on the fluctuation pressure is the full frequency domain. Lengthening the fairing cylinder reduces the fluctuation pressure on the secondary booster downstream of the fairing, and it also affects the reduction of fluctuation energy in the high-frequency domain.

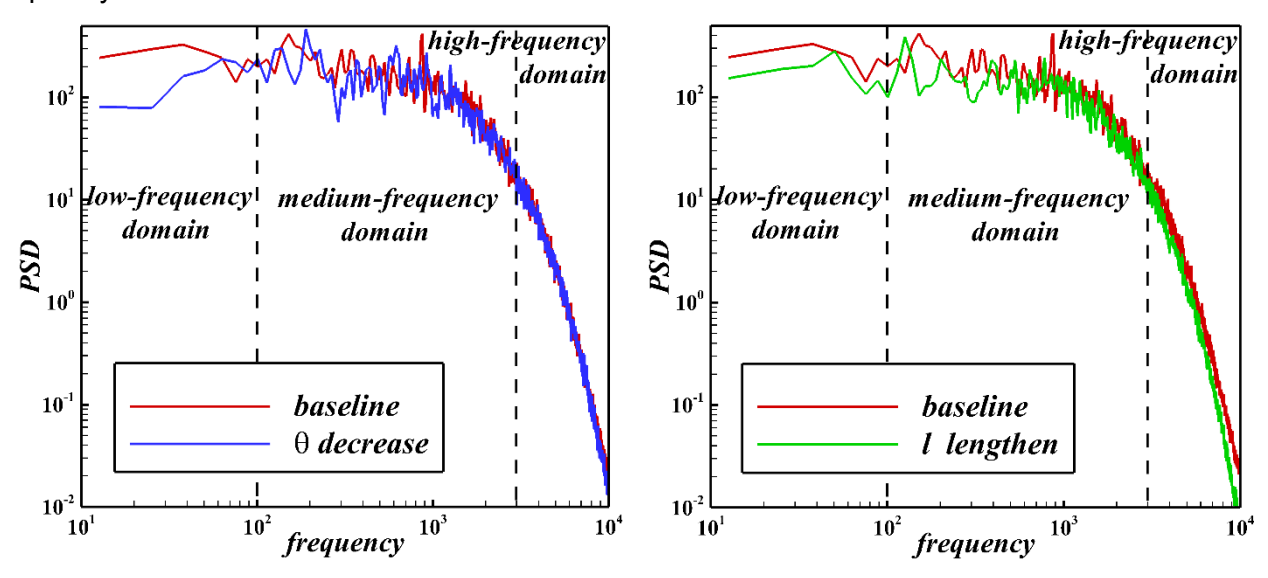


Figure 9 – Power spectral density (PSD) of fluctuation pressure at the peak position of various hammerhead configurations.

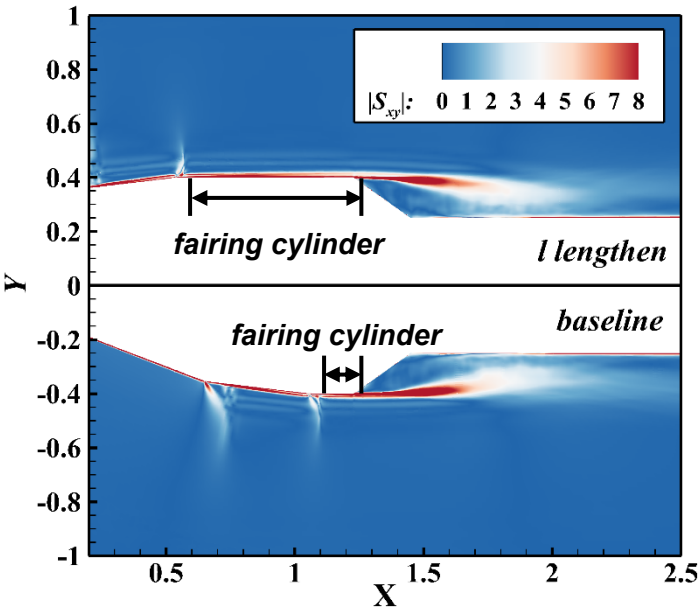


Figure 10 – Time-averaged shear strain rate of the baseline configuration and fairing cylinder length-lengthening configuration.

Figure 10 shows the time-averaged shear strain rate distribution of the baseline configuration and fairing cylinder length-lengthening configuration to investigate the cause of fluctuation load reduction with the full frequency domain. The fluctuation load on the second booster stage is mainly caused by the separation turbulence shedding from the fairing. As shown in Figure 10, the shear strength of the boundary layer flow on the hammerhead configuration with a lengthened fairing cylinder gradually decreases in the process of convection to the boat tail. When the flow reaches the separation point of the boat tail, the shear strength is lower than that of the baseline configuration. The reduction of shear strength weakens the generation of turbulence, resulting in a decrease in the fluctuation energy on the secondary booster generated by the separation turbulence.

In addition, the fluctuation load on the fairing cylinder of the hammerhead model with fairing cylinder lengthening is also reduced, and the reason can be explained in Figure 11. It can be seen from Figure 11 that the perturbation generated by the detached eddies downstream of the fairing has a backscatter effect. The lengthening of the fairing cylinder will decay the perturbation backscatter, resulting in the reduction of fluctuation load upstream of the fairing cylinder.

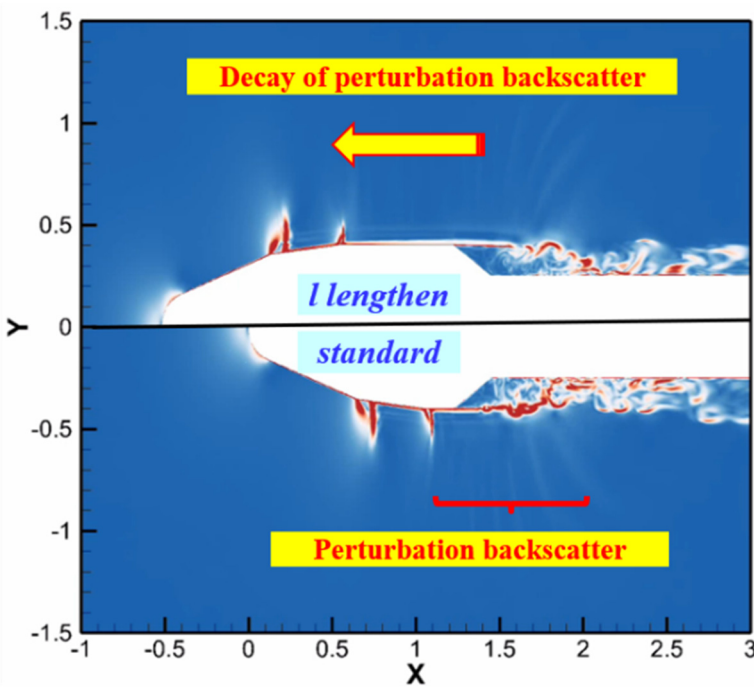


Figure 11 – Perturbation backscatter of various hammerhead models. Flow field is depicted by the density gradient magnitude.

5. Conclusion

The buffeting flow of the hammerhead launch vehicle is numerically investigated by using the recently developed second-moment closure detached-eddy simulation. The frequency domain analysis of hammerhead configuration is carried out to reveal the mechanism of hammerhead launch vehicle buffeting load. Various hammerhead configurations with different fairing geometries have been studied to investigate the effect of the geometric dimensions of the fairing on the launch vehicle fluctuation load. The results show that there exist two dominant sources of buffeting on the launch vehicle: shock wave oscillation on the first stage booster and flow separation and reattachment on the second booster stage downstream of the fairing. The geometric dimension of the fairing investigated in this work mainly affects the buffeting load on the secondary booster downstream of the fairing. Decreasing the boat angle of the fairing can reduce the buffeting load on the secondary booster in the low-frequency domain dominated by the separation bubble pumping mode. The increase of the fairing cylinder length can reduce the shear strength in the free shear layer to weaken the generation of turbulent fluctuation energy, and then achieve the reduction of fluctuation load in the full frequency domain.

6. Acknowledgments

The research was supported by the National Natural Science Foundation of China (No.U2141254, and No.U23B6009). The computations were conducted in Computing Center in Xi'an. The authors thankfully acknowledge these institutions.

7. Contact Author Email Address

Corresponding author email address: wanggang@nwpu.edu.cn

8. Copyright Statement

The authors confirm that they, and/or their company or organization, hold copyright on all of the original material included in this paper. The authors also confirm that they have obtained permission, from the copyright holder of any third party material included in this paper, to publish it as part of their paper. The authors confirm that they give permission, or have obtained permission from the copyright holder of this paper, for the publication and distribution of this paper as part of the ICAS proceedings or as individual off-prints from the proceedings.

References

- [1] Nath B, et al. Alleviation of SWBLI over the payload of a launch vehicle by change of nose shape. *Aerospace Science and Technology*, Vol. 151, No. 1, pp 1-10, 2024.
- [2] Deck S, and Pascal T. Unsteadiness of an axisymmetric separating-reattaching flow: numerical investigation. *Physics of fluids*, Vol. 19, No. 6, pp 1-18, 2007.
- [3] Subbian G, Magrini A, Benini E, Buosi D, Ponza R, and Radespiel R. RANS analysis of HL-CRM at take-off and landing configurations with different flap deflections and engine settings using DLR-TAU code. *AIAA SCITECH 2022 Forum*, San Diego, USA, Vol. 1, AIAA 2022-0048, pp 1-18, 2022.
- [4] Leopardi M, et al. Effects of protuberances on surface loads on the Vega-C launch vehicle. *Journal of Spacecraft and Rockets*, Vol. 16, No. 1, pp 1-14, 2024.
- [5] Park M A, Alauzet F, and Michal T. HLPW-4/GMGW-3: mesh adaptation for RANS technology focus group workshop summary. *Journal of Aircraft*, Vol. 60, No. 4, pp 1-16, 2023.
- [6] Spalart P R. Comments on the feasibility of LES for wings and on the hybrid RANS/LES approach. *The First AFOSR International Conference on DNS/LES*, Louisiana, USA, Vol. 1, pp 1-8, 1997.
- [7] Spalart P R, Deck S, Shur M L, Squires K D, Strelets M K, and Travin A K. A new version of detached-eddy simulation, resistant to ambiguous grid densities. *Theoretical and computational fluid dynamics*, Vol. 20, No. 1, pp 181-195, 2006.
- [8] Shur M. L, Spalart P R, Strelets M K, and Travin A K. A hybrid RANS-LES approach with delayed-DES and wall-modelled LES capabilities. *International journal of heat and fluid flow*, Vol. 29, No. 6, pp 1638-1649, 2008.
- [9] Strelets M. K. Detached eddy simulation of massively separated flows. 39th Aerospace Sciences Meeting and Exhibit, Reno, USA, Vol. 1, AIAA 2001-0879, pp 1-17, 2001.
- [10] Wang G, Li Q Z, and Liu Y. IDDES method based on differential Reynolds-stress model and its application in bluff body turbulent flows. *Aerospace Science and Technology*, Vol. 119, No. 1, pp 1-12, 2021.
- [11] Li Q Z, Chen X, and Wang G. A dynamic version of the improved delayed detached-eddy simulation based on the differential Reynolds-stress model. *Physics of Fluids*, Vol. 34, No. 11, pp 1-15, 2022.
- [12] Liu Y, Wang G, and Zhu H Y, et al. Numerical analysis of transonic buffet flow around a hammerhead payload

- fairing. Aerospace Science and Technology, Vol. 84, No. 1, pp 604-619, 2019.
- [13] Coe, C F., and James B N. Steady and fluctuating pressures at transonic speeds on hammerhead launch vehicles. *NASA Technical Reports*, Vol. 1, No. NASA-TM-X-778, pp1-42, 1962.
- [14] Simon L, Weiss P E, and Deck S. Prediction of wall-pressure fluctuations for separating/reattaching flows applied to space launchers using zonal detached eddy simulation-based convolutional neural networks. *Physics of Fluids*, Vol. 35, No. 6, pp 1-21, 2023.
- [15] Panda J. Verification of calculation procedure for unsteady aerodynamic forces on a launch vehicle. *Journal of Spacecraft and Rockets*, Vol. 56, No. 6, pp 1714-1724, 2019.
- [16] Voegele A P, and Matthew S. Simulating buffet aerodynamics of a hammerhead model using hybrid RANS-LES CFD modeling. *AIAA SCITECH 2023 Forum*, National Harbor, USA, Vol. 1, AIAA 2023-0430, pp 1-23, 2023.
- [17] Wang G, and Ye Z Y. Mixed element type unstructured grid generation and its application to viscous flow simulation. *24th International congress of aeronautical sciences*, Yokohama, Japan, Vol. 1, ICAS 2004-2.4 (St.).R.3, pp 1-8, 2004.
- [18] Li Q Z, Sun X Y, and Wang G. Detached-eddy simulation of the vortex system on the high-lift common research model. *Physics of Fluids*, Vol. 36, No. 2, pp 1-12, 2024.
- [19] Ma B P, Wang G, Ren J, and Ye Z Y. Near-field sonic-boom prediction and analysis with hybrid grid navier–stokes solver. *Journal of Aircraft*, Vol. 55, No. 5, pp 1890-1904, 2018.
- [20] Zhou H, Wang G, Haris H M, and Qin M Z. Fluid-structure coupled analysis of tandem 2D elastic panels. *Aerospace Science and Technology*, Vol. 111, No. 1, pp 1-14, 2021.
- [21] Cécora R D, Radespiel R, Eisfeld B, and Probst A. Differential Reynolds-stress modeling for aeronautics. *AIAA Journal*, Vol. 53, No. 3, pp 739-755, 2015.